FINAL REPORT
"Numerical Computation of Space Shuttle Orbiter Flow Field"
NASA Grant NAG 2-245
ISU-ERI-Ames-89403
CFD-19

FINAL REPORT

NASA GRANT NAG 2-245

October 1, 1983 - May 1, 1988

John C. Tannehill, Principal Investigator
Computational Fluid Dynamics Center
and
Department of Aerospace Engineering

Submitted to:
National Aeronautics and Space Administration
Ames Research Center
Moffett Field, CA

College of Engineering
Iowa State University

A NEW PNS CODE FOR THREE-DIMENSIONAL CHEMICALLY REACTING FLOWS

D. K. Prabhu,* J. C. Tannehill,**
Iowa State University
Ames, Iowa
and
J. G. Marvin†
NASA Ames Research Center
Moffett Field, California

Abstract

A new parabolized Navier-Stokes (PNS) code has been developed to compute the hypersonic, viscous, chemically reacting flow fields around three-dimensional bodies. The flow medium is assumed to be a multicomponent mixture of thermally perfect but calorically imperfect gases. The new PNS code solves the gas dynamic and species conservation equations in a coupled manner using a noniterative, implicit, approximately-factored, finite-difference algorithm. The space-marching method is made well-posed by special treatment of the streamwise pressure gradient term. The code has been used to compute hypersonic laminar flow of chemically reacting air over cones at angles of attack. The results of the computations are compared with the results of reacting boundary-layer computations and show excellent agreement.

Nomenclature

A^*	:	reference area, (m^2)
a_f	:	frozen speed of sound
C_d	:	total drag coefficient
C_f	:	skin-friction coefficient
C_p	:	pressure coefficient
C_{p_f}	:	frozen specific heat of the mixture
c_s	:	mass fraction of species s
D	:	kinematic binary diffusion coefficient
h	:	static enthalpy
H	:	total enthalpy of the mixture
h_s^0	:	enthalpy of formation of species s
K_{b_m}	:	backward reaction rate constant for the mth reaction
K_{f_m}	:	forward reaction rate constant for the mth reaction
L^*	:	reference length, (m)
Le	:	binary Lewis number
$\bar{m}$	:	diffusion mass flux vector
m	:	number of reactions
M_f	:	frozen Mach number
$\mathcal{M}$	:	molecular mass
n	:	number of species
N_A^*	:	Avogadro number, 6.022169 x 10^{26} $(kmol^{-1})$
N_e^*	:	electron number density, (m^{-3})
n_t	:	number of reactants (including catalytic third bodies)
p	:	static pressure of the mixture
$\bar{q}$	:	heat flux vector
$\mathcal{R}^*$	:	universal gas constant, 8314.34 $J/(kmol \cdot K)$
Re	:	Reynolds number based on L^*
St	:	Stanton number
t	:	time
T	:	static temperature of the mixture
u, v, w	:	Cartesian components of the mass-averaged velocity
V	:	magnitude of the mass-averaged velocity
$\dot{w}_s$	:	mass production rate of species s
X_s	:	mole fraction of species s
x, y, z	:	Cartesian coordinates (physical space)
$Z_{r,s}$	:	third body efficiency (relative to argon) of the rth catalytic body
α	:	angle of attack
γ_s	:	mole-mass ratio of species s
θ	:	cone half angle
κ	:	thermal conductivity
μ	:	molecular viscosity
ξ, η, ζ	:	generalized coordinates
ρ	:	mass density
σ	:	safety factor
τ	:	shear stress

Subscripts

i, j, k	:	finite-difference indices
r, s	:	indices denoting species
w	:	wall
x, y, z	:	partial derivative w.r.t. x, y, z
ξ, η, ζ	:	partial derivative w.r.t. ξ, η, ζ
∞	:	freestream

Superscripts

$*$	:	dimensional quantity
c	:	chemical quantity
i	:	inviscid quantity
T	:	transpose
v	:	viscous quantity
x, y, z	:	Cartesian components
ξ, η, ζ	:	transformed components

Introduction

Accurate numerical simulations of the aerothermodynamic environments around the recently proposed hypersonic vehicles[1,2] must account for the various complex relaxation phenomena such as vibrational excitation, chemical reactions, ionization, *etc.*, which occur in the shock

*Research Assistant, Department of Aerospace Engineering. Member AIAA.

**Manager, Computational Fluid Dynamics Center; Professor, Department of Aerospace Engineering. Associate Fellow AIAA.

†Chief, Experimental Fluid Dynamics Branch. Associate Fellow AIAA.

layers. The numerical simulation of complete thermochemical nonequilibrium has been successfully accomplished by Park[3,4] for one-dimensional flows. The extension of this analysis to higher dimensional flows is quite complicated and requires further research. However, as a first step, the problem can be simplified by assuming the flow field to be in thermal equilibrium but not in chemical equilibrium. The numerical simulation of viscous, chemically reacting, external flows around three-dimensional configurations is the focus of attention of several investigations today.

The numerical methods currently employed fall into two main categories, (i) time-marching methods and (ii) space-marching methods. In the time-marching methods,[5-8] time-asymptotic solutions to the Navier-Stokes equations are computed. These methods are accurate but require a substantial amount of computer time. Space-marching methods, on the other hand, require much less computer time and provide accurate solutions in cases where they are applicable. In the latter category, the viscous shock-layer (VSL) equations [9,10] have been widely used to compute three-dimensional, viscous, chemically reacting flows. These equations are uniformly valid in the shock layer but fail in the presence of crossflow separation. This deficiency is overcome through the use of the parabolized Navier-Stokes (PNS) equations. Bhutta and Lewis[11] were one of the first to use the PNS equations to compute chemical nonequilibrium flow fields. They solved the chemistry and gas dynamics separately and used an iterative approach to couple the two. In contrast to their approach, Prabhu *et al.*[12] developed a chemical nonequilibrium PNS code in which the gas dynamics and chemistry were solved simultaneously in a noniterative manner. This two-dimensional/axisymmetric code was successfully applied to reacting flows over wedges and cones and was found to be very competitive in terms of both efficiency as well as computing time. Having established the feasibility of computing reacting flows with a coupled approach, a new PNS code for three-dimensional bodies has been developed in the present study.

The present paper describes in detail the development of this new PNS code which can compute chemically reacting flow fields around three-dimensional bodies. As in the previous study[12], the gas dynamic and species conservation equations are solved in a coupled manner. A noniterative, implicit, approximately-factored, finite-difference method is used to solve the PNS equations. The flow medium considered in the present computations is air consisting of six species and electrons. The electrons are eliminated from the species set using the principle of conservation of charge. The source terms are treated in a partially implicit manner in the present formulation. The code has been used to compute a number of chemically reacting flow fields around cones at angles of attack. The results of the computations are compared with those of a reacting boundary-layer code.[13]

Governing Equations

The equations governing the steady, three-dimensional laminar flow of a multicomponent gas have been obtained from the equations in Ref. 14 by (i) neglecting the time-derivative terms, (ii) assuming the flow to be in thermal equilibrium, (iii) neglecting radiation, and by (iv) assuming mass diffusion to be binary and due to concentration gradients only. These equations can be written in nondimensional, strong conservation-law form in Cartesian coordinates for an n-component system as:

$$\mathbf{E}^i_x + \mathbf{F}^i_y + \mathbf{G}^i_z = \frac{1}{Re}\left(\mathbf{E}^v_x + \mathbf{F}^v_y + \mathbf{G}^v_z\right) + \mathbf{W}^c \qquad (1)$$

The $(n+4)$-component vector of conservation variables $\mathbf{Q}$ is chosen as

$$\mathbf{Q} = \left\{\rho, \rho u, \rho v, \rho w, \rho H, \rho c_1, \rho c_2, \ldots, \rho c_{n-1}\right\}^T \qquad (2)$$

$\mathbf{E}^i$, $\mathbf{F}^i$, and $\mathbf{G}^i$ are the $(n+4)$-component inviscid flux vectors. $\mathbf{E}^v$, $\mathbf{F}^v$, and $\mathbf{G}^v$ are $(n+4)$-component viscous flux vectors. $\mathbf{W}^c$ is the vector of chemical source terms. All these vectors are functions of the elements of the vector $\mathbf{Q}$ and their spatial derivatives. Explicit expressions for elements of the flux and source vectors are given in Appendix A. Note that the vector of dependent variables contains both the fluid dynamic and chemistry variables and that only $(n-1)$ of the n species continuity equations are required because the mass fractions sum to unity. Thus, the nth species continuity equation is replaced by the following algebraic equation

$$c_n = 1 - \sum_{s=1}^{n-1} c_s \qquad (3)$$

In addition to the above equations, the following equations are also used

$$p = \frac{\beta_1 \rho T}{M} \qquad (4)$$

$$H = h + \frac{1}{2}(u^2 + v^2 + w^2) \qquad (5)$$

$$M = \left(\sum_{s=1}^{n} \frac{c_s}{M_s}\right)^{-1} \qquad (6)$$

where Eq. 4 is the equation of state for perfect gases, Eq. 5 is the definition of the mixture total enthalpy and Eq. 6 is the definition of the mixture molecular mass.

The following nondimensionalization has been employed in the present formulation

$$\begin{aligned}
x, y, z &= \frac{x^*, y^*, z^*}{L^*} & p &= \frac{p^*}{\rho^*_\infty V^{*2}_\infty} & \dot{w}_s &= \frac{\dot{w}^*_s L^*}{\rho^*_\infty V^*_\infty} \\
u, v, w &= \frac{u^*, v^*, w^*}{V^*_\infty} & h &= \frac{h^*}{V^{*2}_\infty} & \mu &= \frac{\mu^*}{\mu^*_\infty} \\
\rho &= \frac{\rho^*}{\rho^*_\infty} & M &= \frac{M^*}{M^*_\infty} & \kappa &= \frac{\kappa^*}{\kappa^*_\infty} \\
T &= \frac{T^*}{T^*_\infty} & C_{p_f} &= \frac{C^*_{p_f} T^*_\infty}{V^{*2}_\infty} & D &= \frac{D^*}{D^*_\infty}
\end{aligned} \qquad (7)$$

The other nondimensional quantities appearing in the equations are

$$\begin{aligned}
Re &= \frac{\rho^*_\infty V^*_\infty L^*}{\mu^*_\infty} & \beta_2 &= \frac{\kappa^*_\infty T^*_\infty}{\mu^*_\infty V^{*2}_\infty} \\
\beta_1 &= \frac{R^* T^*_\infty}{M^*_\infty V^{*2}_\infty} & \beta_3 &= \frac{\rho^*_\infty D^*_\infty}{\mu^*_\infty}
\end{aligned} \qquad (8)$$

In order to close the system of governing equations, the thermodynamic and transport properties of the constituent gases and the mixture are required. This is discussed in the next subsection.

Gas Model, Thermodynamic and Transport Properties

(a) Gas Model

The chemical model used in the present calculations is air consisting of molecular oxygen (O_2), atomic oxygen (O), molecular nitrogen (N_2), nitric oxide (NO), nitric oxide ion (NO^+), atomic nitrogen (N), and electrons (e^-). These species are indexed $s = 1 - 6$ in the order shown with the electrons being treated as a special case. The following reactions are considered between the constituent species

$$
\begin{aligned}
&(1)\quad O_2 + M_1 \rightleftharpoons 2O + M_1\\
&(2)\quad N_2 + M_2 \rightleftharpoons 2N + M_2\\
&(3)\quad N_2 + N \rightleftharpoons 2N + N\\
&(4)\quad NO + M_3 \rightleftharpoons N + O + M_3\\
&(5)\quad NO + O \rightleftharpoons O_2 + N\\
&(6)\quad N_2 + O \rightleftharpoons NO + N\\
&(7)\quad N + O \rightleftharpoons NO^+ + e^-
\end{aligned}
$$

where M_1, M_2, and M_3 are catalytic third bodies. The above model has six species ($n = 6$), seven reactions ($m = 7$) and ten reactants ($n_t = 10$) including electrons. The reaction rates have been obtained from Blottner.[18]

(b) Specific Heat and Enthalpy

The enthalpies (J/kg) and specific heats ($J/kg \cdot K$) of the species are obtained from the following relations

$$
\begin{aligned}
h_s^* &= T^* \cdot C_{1,s}(T^*) + h_s^{0*}\\
C_{p,s}^* &= C_{2,s}(T^*)
\end{aligned}
\tag{9}
$$

Tables of $C_{1,s}$ and $C_{2,s}$ as functions of T^* (K) are obtained from Ref. 13. Cubic spline interpolation is used in these tables. The enthalpy and frozen specific heat of the mixture are given by the following expressions

$$
h^* = \sum_{s=1}^{n} c_s h_s^* \tag{10}
$$

$$
C_{p_f}^* = \left.\frac{dh^*}{dT^*}\right|_{c_1,\ldots,c_n} = \sum_{s=1}^{n} c_s \frac{dh_s^*}{dT^*} = \sum_{s=1}^{n} c_s C_{p,s}^* \tag{11}
$$

where the subscripts on the differentiation indicate that the composition of the mixture is frozen locally.

(c) Viscosity and Thermal Conductivity

The viscosity ($N \cdot s/m^2$) of species s is calculated from curve fits developed in Ref. 13. These curve fits are of the form

$$
\mu_s^* = 0.1 \exp\left[A_s (\log_e T^*)^2 + B_s \log_e T^* + C_s\right] \tag{12}
$$

where A_s, B_s, and C_s are constants. The thermal conductivity ($W/m \cdot K$) of species s is computed using Eucken's semiempirical formula

$$
\kappa_s^* = \frac{\mu_s^* R^*}{M_s^*}\left(C_{p,s}^* \frac{M_s^*}{R^*} + \frac{5}{4}\right) \tag{13}
$$

The viscosity and thermal conductivity of the mixture are calculated using Wilke's semiempirical mixing rule[15]

$$
\mu^* = \sum_{s=1}^{n} \frac{X_s \mu_s^*}{\phi_s}, \qquad \kappa^* = \sum_{s=1}^{n} \frac{X_s \kappa_s^*}{\phi_s} \tag{14}
$$

where

$$
X_s = \frac{c_s M^*}{M_s^*} \tag{15}
$$

$$
\phi_s = \sum_{r=1}^{n} X_r \left[1 + \sqrt{\frac{\mu_s^*}{\mu_r^*}}\left(\frac{M_r^*}{M_s^*}\right)^{1/4}\right]^2 \left[\sqrt{8}\sqrt{1 + \frac{M_s^*}{M_r^*}}\right]^{-1} \tag{16}
$$

Wilke's mixing rule is considered adequate for weakly ionizing flows.

(d) Diffusion Coefficient

The binary Lewis numbers for all the species are assumed to be the same constant Le. The kinematic binary diffusion coefficient D^* (m^2/s) is then computed from the definition

$$
D^* = \frac{\kappa^* Le}{\rho^* C_{p_f}^*} \tag{17}
$$

The dimensional thermodynamic and transport properties are nondimensionalized using Eq. 7 prior to their use in the code.

Coordinate Transformation

Consider a generalized transformation of the spatial coordinates as shown below

$$
\xi = \xi(x, y, z), \quad \eta = \eta(x, y, z), \quad \varsigma = \varsigma(x, y, z) \tag{18}
$$

where ξ is the "streamwise" coordinate, η is the "normal" coordinate and ς is the "circumferential" coordinate. Using this transformation, the governing equations can be recast into the strong conservation form given by

$$
\hat{\mathbf{E}}_\xi^i + \hat{\mathbf{F}}_\eta^i + \hat{\mathbf{G}}_\varsigma^i = \frac{1}{Re}\left(\hat{\mathbf{E}}_\xi^v + \hat{\mathbf{F}}_\eta^v + \hat{\mathbf{G}}_\varsigma^v\right) + \hat{\mathbf{W}}^c \tag{19}
$$

where $\hat{\mathbf{E}}^i$, $\hat{\mathbf{F}}^i$, $\hat{\mathbf{G}}^i$, $\hat{\mathbf{E}}^v$, $\hat{\mathbf{F}}^v$, $\hat{\mathbf{G}}^v$, and $\hat{\mathbf{W}}^c$, are the transformed inviscid and viscous fluxes and chemical source terms, respectively. Their forms are given in Appendix A.

The equation set, Eq. 19, is simplified by making the thin-layer approximation, *i.e.*, the viscous and diffusion effects in the streamwise and meridional directions are assumed to be negligibly small compared to those in the normal direction. Therefore, the set of equations is simplified to

$$
\hat{\mathbf{E}}_\xi^i + \hat{\mathbf{F}}_\eta^i + \hat{\mathbf{G}}_\varsigma^i = \frac{1}{Re}\hat{\mathbf{F}}_\eta^v + \hat{\mathbf{W}}^c \tag{20}
$$

where $\hat{\mathbf{F}}^v$ contains derivatives with respect to the η coordinate only.

Streamwise Pressure Gradient

In its present form, Eq. 20, is hyperbolic-elliptic in the streamwise or marching direction ξ and consequently the

space-marching method of solution is ill-posed. The technique used to overcome this problem was originally proposed by Vigneron *et al.*[10] for ideal gases and later extended to chemically reacting flows by Prabhu *et al.*[12] Using this technique it was found that the governing equations are hyperbolic-parabolic if and only if (i) there is no axial flow separation in the solution domain, (ii) the local frozen Mach number is greater than unity in the inviscid part of the flow field, and (iii) only a fraction ω of the streamwise pressure gradient $\partial p/\partial \xi$ is retained in the subsonic part of the flow field. The magnitude of ω depends on the local frozen Mach number and is determined from the expression

$$\omega = \min\left\{1, \sigma M_f^{\xi^2}\left[1 + \chi(M_f^{\xi^2} - 1)\right]^{-1}\right\} \tag{21}$$

where σ ($0.8 \le \sigma \le 0.9$) is a factor of safety and

$$\chi = \frac{\beta_1}{\mathcal{M} C_{p_f}} \tag{22}$$

$$M_f^{\xi} = \left[(\frac{\xi_x}{J})u + (\frac{\xi_y}{J})v + (\frac{\xi_z}{J})w\right] / \left[a_f |\frac{\nabla \xi}{J}|\right] \tag{23}$$

$$a_f^2 = \frac{\lambda}{(1-\lambda)} C_{p_f} T \tag{24}$$

Introducing ω into Eq. 20, the streamwise inviscid flux can be split as follows

$$\mathbf{E}^i = \bar{\mathbf{E}}^{i'} + \bar{\mathbf{E}}^{i''} \tag{25}$$

where

$$\bar{\mathbf{E}}^{i''} = (1-\omega)p\{0, \frac{\xi_x}{J}, \frac{\xi_y}{J}, \frac{\xi_z}{J}, 0, 0, 0, \ldots, 0\}^T \tag{26}$$

Using Eq. 26, Eq. 20 can be rewritten as

$$\bar{\mathbf{E}}^{i'}_{\xi} + \bar{\mathbf{F}}^i_{\eta} + \bar{\mathbf{G}}^i_{\zeta} = \frac{1}{Re}\bar{\mathbf{F}}^v_{\eta} + \bar{\mathbf{W}}^c - \bar{\mathbf{E}}^{i''}_{\xi} \tag{27}$$

Further, the last term of Eq. 27 is normally neglected in the subsonic region. Hence the final set of equations that is solved is

$$\bar{\mathbf{E}}^{i'}_{\xi} + \bar{\mathbf{F}}^i_{\eta} + \bar{\mathbf{G}}^i_{\zeta} = \frac{1}{Re}\bar{\mathbf{F}}^v_{\eta} + \bar{\mathbf{W}}^c \tag{28}$$

Numerical Solution of PNS Equations

Finite-difference Algorithm

The numerical algorithm used to solve the system of equations, Eq. 28, is an adaptation of the one developed by Tannehill *et al.*[17] The factored algorithm is implemented as the following sequence of steps

(a) Normal Sweep: $k = 2, 3, \ldots, NK$

$$\left\{\hat{\mathbf{A}}_{i,k,j} - \Delta\xi\hat{\mathbf{A}}^{\xi}_{i,k,j} + \Delta\xi\frac{\partial}{\partial\zeta}(\hat{\mathbf{C}}_{i,k,j})\right\}\Delta\hat{\mathbf{Q}}_{i,k,j} =$$

$$-\Delta\xi\frac{\partial\bar{\mathbf{E}}^{i'}}{\partial\xi}\Big|_Q - \Delta\xi\left[\frac{\partial}{\partial\eta}\left(\hat{\mathbf{F}}^i_{i,k,j} - \frac{1}{Re}\hat{\mathbf{F}}^v_{i,k,j}\right) + \frac{\partial}{\partial\zeta}\left(\hat{\mathbf{G}}^i_{i,k,j}\right)\right] - \Delta\xi\hat{\mathbf{W}}^c_{i,k,j} \tag{29}$$

(b) Circumferential Sweep: $j = 1, 2, \ldots, NJ$

$$\left\{\hat{\mathbf{A}}_{i,k,j} - \Delta\xi\hat{\mathbf{A}}^{\xi}_{i,k,j} + \Delta\xi\frac{\partial}{\partial\eta}(\hat{\mathbf{B}}_{i,k,j} - \frac{1}{Re}\hat{\mathbf{M}}_{i,k,j})\right\}\Delta\mathbf{Q}_{i,k,j} = (\hat{\mathbf{A}}_{i,k,j} - \Delta\xi\hat{\mathbf{A}}^{\xi}_{i,k,j})\Delta\hat{\mathbf{Q}}_{i,k,j} \tag{30}$$

(c) Update:

$$\mathbf{Q}_{i+1,k,j} = \mathbf{Q}_{i,k,j} + \Delta\mathbf{Q}_{i,k,j} \tag{31}$$

where the Jacobian matrices are

$$\hat{\mathbf{A}} = \frac{\partial\bar{\mathbf{E}}^{i'}}{\partial\mathbf{Q}}, \quad \hat{\mathbf{B}} = \frac{\partial\bar{\mathbf{F}}^i}{\partial\mathbf{Q}}, \quad \hat{\mathbf{C}} = \frac{\partial\bar{\mathbf{G}}^i}{\partial\mathbf{Q}}, \quad \hat{\mathbf{M}} = \frac{\partial\bar{\mathbf{F}}^v}{\partial\mathbf{Q}}, \quad \hat{\mathbf{A}}^c = \frac{\partial\bar{\mathbf{W}}^c}{\partial\mathbf{Q}} \tag{32}$$

The subscripts i, k, j are indices associated with the directions ξ, η, ζ, respectively. NJ and NK are the total number of grid points in the ζ and η directions, respectively. $\Delta\xi$ is the marching stepsize. The derivatives $\partial/\partial\eta$ and $\partial/\partial\zeta$ are replaced by conventional three-point central-difference operators. The algorithm is first-order accurate in the ξ direction and second-order accurate in the η and ζ directions. Freestream fluxes are subtracted from the inviscid fluxes in order to preserve freestream. Fourth-difference explicit and second-difference implicit smoothing operators are also added to the factored operators. These have not been shown above but their forms can be found in Ref. 12.

The Jacobian matrices $\hat{\mathbf{A}}$, $\hat{\mathbf{B}}$, $\hat{\mathbf{C}}$, $\hat{\mathbf{M}}$, and $\hat{\mathbf{A}}^c$ represent the linearisation of the fluxes and source terms and the elements of these matrices are given in Appendices B, C, and D. In the linearization of the viscous flux, the transport properties are assumed to be locally constant. The caret above the symbols for the fluxes, Jacobians, and source terms signifies that the geometry is not linearized along with the flow variables.

The left hand sides of Eqs. 29 and 30 correspond to a block-tridiagonal system of equations. The blocks are square matrices of order $(n + 4)$. For the six-species air model considered in the present calculations, the blocks are square matrices of order 10. The block-tridiagonal solver for the 10 x 10 blocks is developed along the same lines as the one by Steger[18] for 5 x 5 blocks.

Boundary Conditions

In the present work, only flows without yaw are considered. Therefore, at every streamwise station the computational domain is bounded by (i) the outer boundary which is taken to be the freestream, (ii) the inner boundary which is taken to be the wall, and (iii) the pitch plane of symmetry. Any discontinuities in the flowfield are "captured" as a part of the solution.

At the pitch plane of symmetry reflection boundary conditions are imposed and thus, flow symmetry is maintained.

The following nondimensional boundary conditions are imposed implicitly at the wall

(a) $u = 0,\ v = 0,\ w = 0,\ \frac{\partial}{\partial n}(p) = 0$

(b) $T = T_w$ (isothermal wall) or $\frac{\partial}{\partial n}(T) = 0$ (adiabatic wall)

(c) $c_s = c_{s_\infty}$ (catalytic wall) or $\frac{\partial}{\partial n}(c_s) = 0$ (noncatalytic wall), $s = 1, 2, \ldots, n-1$

The nondimensional boundary conditions at the outer boundary are

(a) $u = \cos\alpha,\ v = 0,\ w = \sin\alpha$

(b) $T = 1,\ \rho = 1,\ c_s = c_{s_\infty},\ s = 1, 2, \ldots, n-1$

Initial Conditions

The PNS equations require initial conditions in addition to the boundary conditions. The usual procedure is to use an initial data surface generated by a full Navier-Stokes code. For conical or pointed bodies, however, the code generates it own starting solution. This starting solution is generated iteratively using a "stepback" procedure.[12,19]

Decoding

The primitive variables $\rho, u, v, w, H, c_1, c_2, \ldots, c_{n-1}$ at station $i+1$ are easily obtained from the elements of $\mathbf{Q}$. The mass fraction of the nth species is computed using Eq. 3 and the static enthalpy of the mixture is computed using Eq. 5. For a given species distribution $c_1, c_2, \ldots, c_n$ and mixture enthalpy h, the temperature is iteratively determined using the following algorithm[12]

$$T^{k+1} = T^k - \frac{\sum_{s=1}^{n} c_s h_s(T^k) - h}{\sum_{s=1}^{n} c_s C_{p,s}(T^k)} \tag{33}$$

where k is the index of iteration. The iterations are continued until

$$|T^{k+1} - T^k| \leq \epsilon \tag{34}$$

where ϵ is a small positive quantity. Once the temperature is determined, the thermodynamic and transport properties are easily computed using the expressions given in the previous sections.

Grid Generation

An algebraic grid generation procedure is used in the present calculations. In this procedure, the point on the body surface and the point on the outer boundary are connected by a straight line and the grid points are distributed on this line using the following stretching function

$$s(\eta) = 1 - \beta\left\{\frac{(\beta+1)^{1-\eta} - (\beta-1)^{1-\eta}}{(\beta+1)^{1-\eta} + (\beta-1)^{1-\eta}}\right\} \tag{35}$$

$$\eta = \frac{(k-1)}{(NK-1)} \qquad k = 1, 2, \ldots, NK \tag{36}$$

where β ($\beta > 1$) is the stretching parameter and NK is the total number of points on the grid line. Note that $s(0) = 0$ and $s(1) = 1$ and the points are clustered close to the wall for values of β close to 1. Such clustering is necessary for good resolution of the subsonic viscous layer.

The coordinates of the grid points are then obtained from

$$\begin{aligned} x &= x_w + n_1 s(\eta)\delta(\xi) \\ y &= y_w + n_2 s(\eta)\delta(\xi) \\ z &= z_w + n_3 s(\eta)\delta(\xi) \end{aligned} \tag{37}$$

where n_1, n_2, and n_3 are the direction cosines of the unit vector along the grid line and δ is the linear distance of the outer boundary from the body surface.

The metrics are then computed using first-order accurate one-sided differences in the ξ direction and second-order accurate central-differences in the η and ζ directions.

Results

In order to validate the present nonequilibrium PNS code, two test cases were computed. The coordinate system employed in the present calculations is shown in Fig. 1.

Test Case 1

The first test case computed was that of hypersonic laminar flow of dissociating air over a 10 degree cone at 0 degree angle of attack. The altitude chosen was 60.96 km where the ambient pressure and temperature are 20.35 N/m^2 and 252.6 K, respectively. The remaining flow conditions are

$V_\infty = 8100\ m/s$

$T_\infty = 1200\ K$ and noncatalytic wall

$c_{1_\infty} = 0.2629$ and $c_{3_\infty} = 0.7371$

$\mathcal{L}e = 1.4$

The computation was started at $x = 1.5 \times 10^{-3}$ using the initial solution generated by the "stepback" procedure. The solution was then marched to $x = 3.5$. The marching step size was chosen to be $\Delta\xi = f\delta_s$ where $f > 1$ and δ_s is the maximum thickness of the subsonic layer (in the present calculations, a value of 2 was assigned to f). The grid used in the calculations consisted of 67 points in the normal direction and 21 points in the meridional direction. The distance of the first point away from the body surface was varied linearly from 3×10^{-5} to 2.3×10^{-4} which determined the appropriate stretching parameter β. The grid lines were placed normal to the body and the height of the outer boundary was kept fixed at 0.5. The edge of the boundary layer was located approximately using total enthalpy as the criterion. The edge values of pressure, temperature and velocity at the last station were then used as the uniform edge conditions for the reacting boundary-layer (RBL) code of Ref. 13.

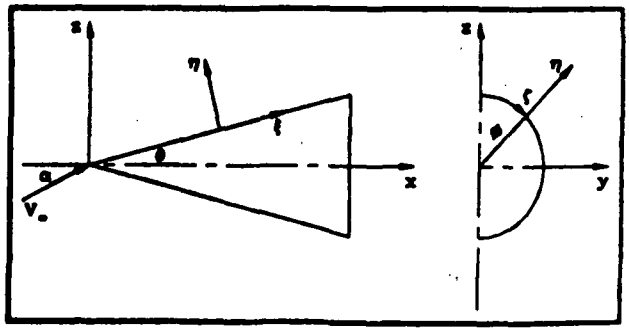

Fig. 1 Coordinate system.

The surface pressure coefficient is defined as

$$C_p = \frac{p_w - p_\infty}{\frac{1}{2}\rho_\infty V_\infty^2} \tag{38}$$

In Fig. 2, the axial variation of the surface pressure coefficient is compared against the edge pressure of the boundary-layer code. The pressure predicted by the PNS code is initially higher than the edge pressure of the RBL code but eventually asymptotes to the latter value. The higher pressure is believed due to the leading edge effect. It must be recalled here that the PNS equations contain a normal momentum equation. This permits the interaction of the outer inviscid region with the inner viscous region. At the altitude considered, this interaction is fairly strong because the Reynolds number is low. Consequently, the pressure is higher. As the solution proceeds downstream, the interaction is reduced and one obtains near boundary-layer behavior. The increase in pressure leads to some differences between the PNS and boundary-layer results as will be discussed later.

The PNS equations are uniformly valid in the shock layer and as mentioned earlier the solution domain includes both the viscous and inviscid regions. In Figs. 3-8 only 20 percent of the solution domain is shown in order to emphasize the details of the viscous boundary layer. Pitch plane profiles of tangential velocity and temperature at $x = 3.5$ are compared in Figs. 3 and 4, respectively. The agreement between the two codes is excellent. Mass fraction profiles of O and NO at $x = 3.5$ are compared in Figs. 5 and 6, respectively. The mass fractions have been normalized using the corresponding wall values. The agreement between the two codes is again excellent. The wall values of the mass fractions were also found to be in very good agreement. The electron density (number of electrons per m^3) is obtained from the mass fraction of the NO^+ ion. This follows from charge conservation and is defined as

$$N_e = \frac{\rho c_{NO^+} N_A}{M_{NO^+}} \tag{39}$$

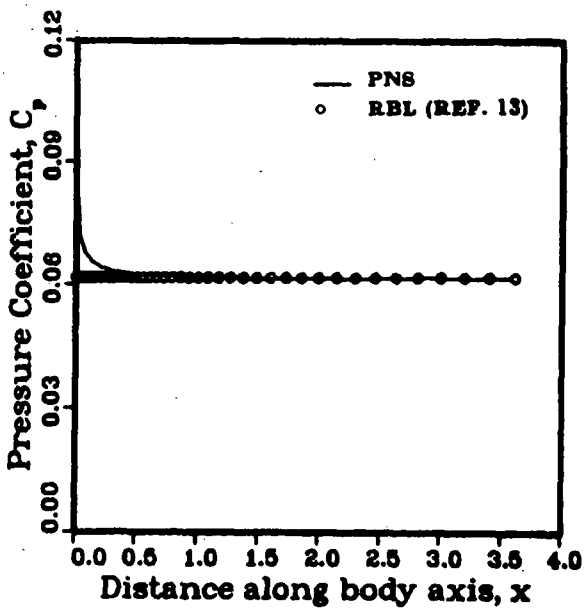

Fig. 2 Wall pressure coefficient comparison.

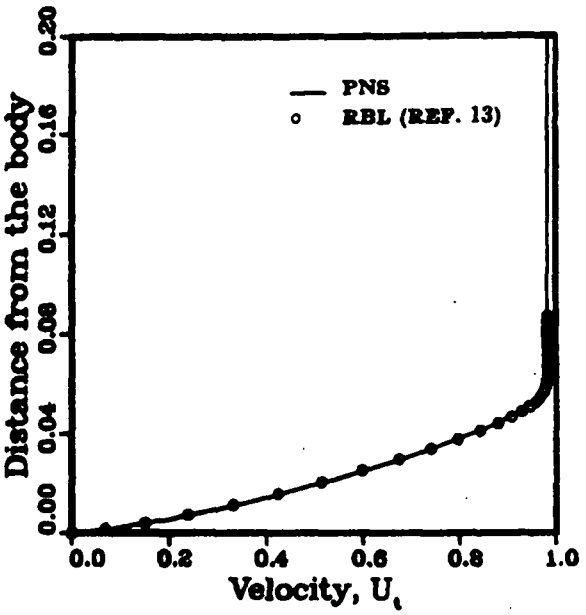

Fig. 3 Tangential velocity profiles at $x = 3.5$.

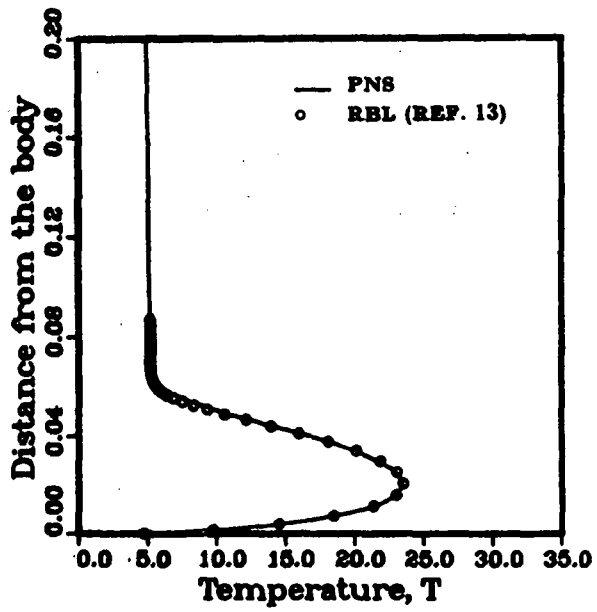

Fig. 4 Temperature profiles at $x = 3.5$.

In Figs. 7 and 8, profiles of the mass fraction of NO^+ and electron density obtained are compared. Again, the mass fractions and densities have been normalized using the corresponding wall values. The curve corresponding to the PNS calculations passes below the symbols representing the boundary-layer calculations. This is due to the fact that the PNS code predicts a higher amount of NO^+ near the wall. The onset of chemical reactions occurs earlier in the PNS code than in the RBL code because of the initial high pressures. This effect persists downstream and hence the disparity. The electron densities have been obtained from the mass fractions of NO^+ and consequently these densities will exhibit an identical behavior.

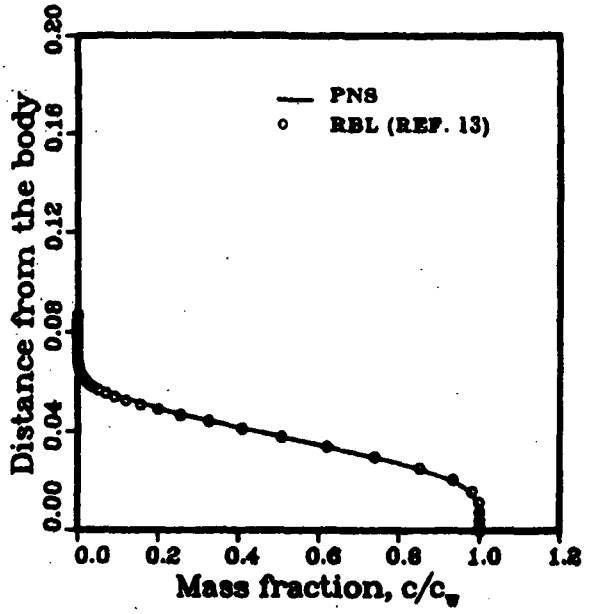

Fig. 5 O mass fraction profiles at $x = 3.5$.

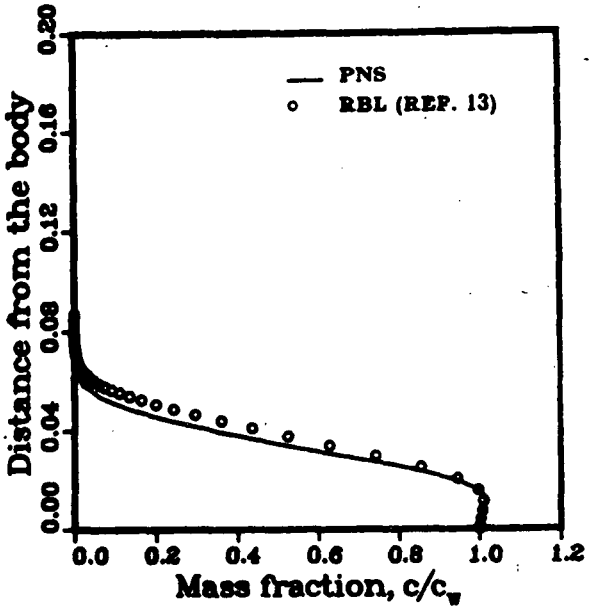

Fig. 7 NO^+ mass fraction profiles at $x = 3.5$.

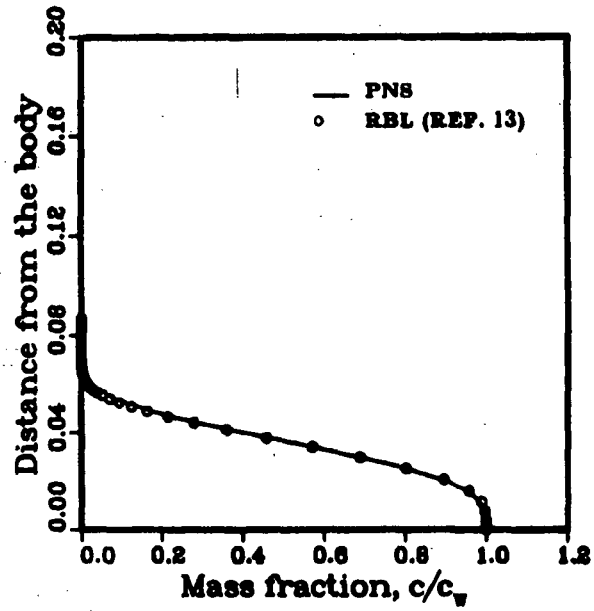

Fig. 6 NO mass fraction profiles at $x = 3.5$.

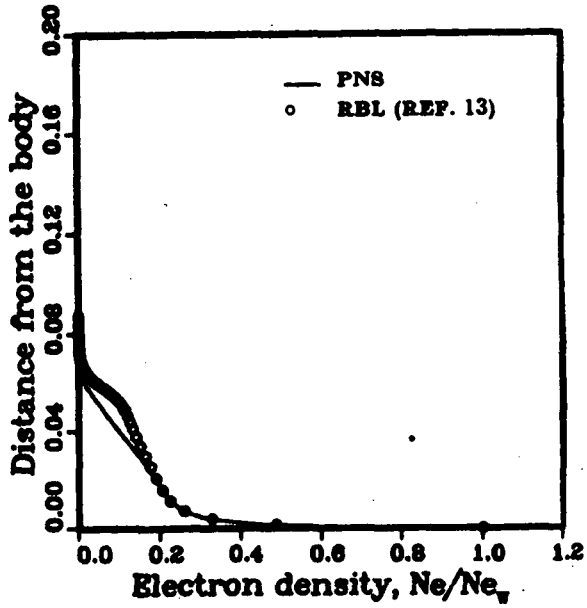

Fig. 8 Electron density profiles at $x = 3.5$.

The skin-friction coefficient and the Stanton number are defined as:

$$C_f = \frac{\tau_w}{\frac{1}{2}\rho_\infty V_\infty^2} \tag{40}$$

$$St = \frac{-q_w}{\rho_\infty V_\infty (H_\infty - H_w)} \tag{41}$$

where the wall shear stress (N/m^2) is computed from

$$\tau_w = -\mu_w \left.\frac{\partial V}{\partial n}\right|_w \tag{42}$$

and the total heat transfer (W/m^2) is computed from

$$q_w = -\kappa_w \left.\frac{\partial T}{\partial n}\right|_w - \rho_w D_w \sum_{s=1}^{n} h_s \left.\frac{\partial c_s}{\partial n}\right|_w \tag{43}$$

The first term in Eq. 43 is the conductive heating rate and the second the diffusive heating rate. The partial derivative, $\partial/\partial n$, is taken in the direction normal to the surface of the body. In Figs. 9 and 10, the skin-friction coefficient and Stanton number are plotted as functions of the distance along the cone axis. The coefficients predicted by the two codes are in very good agreement.

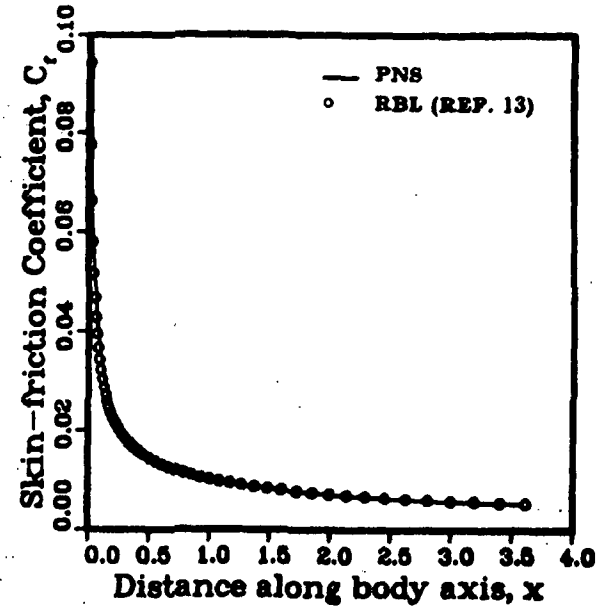

Fig. 9 Skin-friction coefficient comparison.

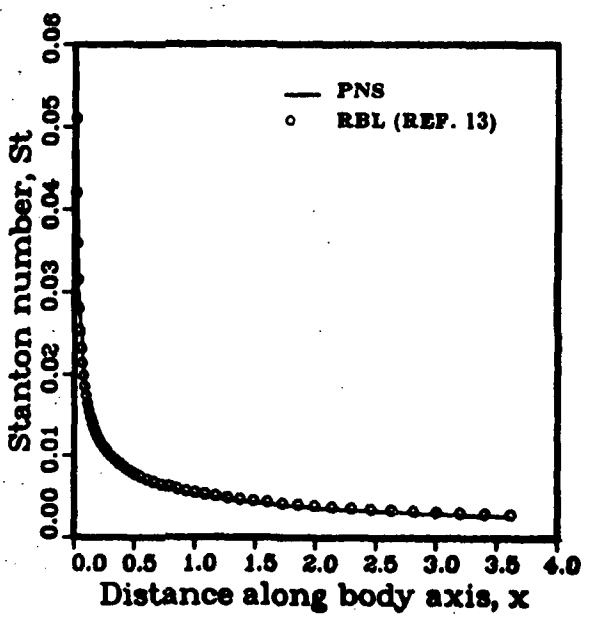

Fig. 10 Heat transfer coefficient comparison.

The total drag coefficient is defined as

$$C_d = \frac{D^*}{\frac{1}{2}\rho_\infty^* V_\infty^{*2} A^*} \tag{44}$$

where D^* (N) is the total drag, i.e., the sum of the pressure drag and the skin-friction drag. The base pressure drag has been neglected. In the present study, trapezoidal integration was used to compute the total drag. The cross-sectional area at $x = 3.5$ was chosen as the reference area. The value of the drag coefficient predicted by the PNS code was 0.1037 which is in very good agreement (less than 1 percent) with the value of 0.1043 predicted by the RBL code.

The ideal gas and equilibrium air models represent two physical extremes. In the former case, there are no reactions (infinitely slow reactions) and in the latter case, the reactions proceed at an infinite rate. In the gas model considered in the present calculations, the reactions proceed at finite-rate and hence is between these two extremes. In order to demonstrate this, the PNS code of Ref. 20 was modified and specialized to two-dimensional and axisymmetric bodies. New curve fits[21] for the thermodynamic properties of equilibrium air were used in the code. For the ideal gas calculations the ratio of specific heats was set to 1.4. The code was then used to compute the flow around the 10 deg. cone for the same freestream conditions. In Fig. 11, the temperature profiles at $x = 3.5$ obtained for the three gas models are compared. It is evident from the figure that the peak temperature for the finite-rate chemistry case lies between the peaks for the ideal gas and equilibrium air models. In the ideal gas case there are no internal degrees of freedom for the energy to be stored. For the finite-rate reaction case, some of the energy goes into exciting the internal degrees of freedom and some into chemical reactions. This effectively lowers the peak temperature. For the equilibrium air gas, thermochemical equilibrium is acheived instantaneously at every point of the flow field and hence a much lower peak temperature. In Fig. 12, the effect of the three gas models on the Stanton number is shown. The Stanton number has been plotted as a function of the axial distance. The equilibrium Stanton number is slightly greater than the finite-rate chemistry model which in turn is greater than the ideal gas Stanton number.

Test Case II

In order to validate the angle of attack capability of the code, a simple test case was chosen. In this test case, hypersonic laminar flow of reacting air over a 10 degree cone

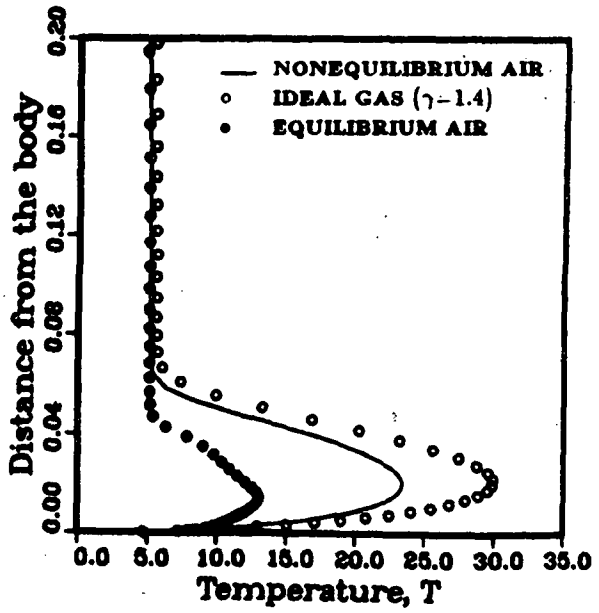

Fig. 11 Effect of gas models on temperature. Temperature profiles at $x = 3.5$.

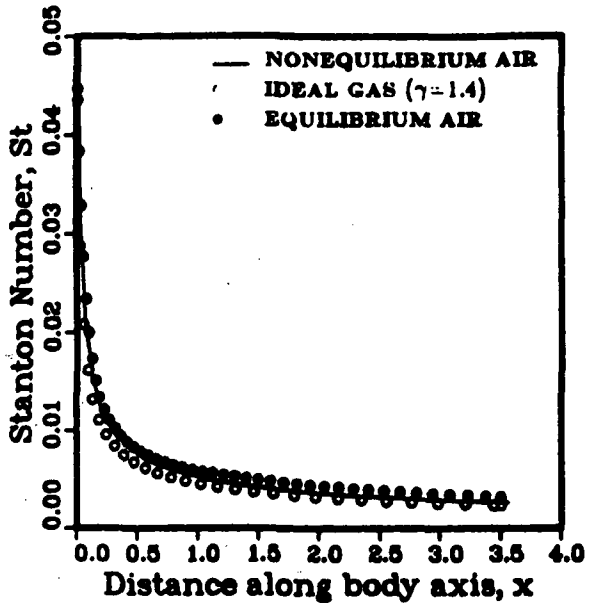

Fig. 12 Effect of gas models on Stanton number. Axial variation of Stanton number.

at 2.5 , 5, 7.5 and 10 degrees angle of attack was computed. The flow conditions for these calculations were the same as the flow conditions for Test Case 1. The starting solution for the PNS code for each angle of attack was obtained using the stepback procedure with the guessed initial solution being the freestream. The mesh spacing on the windside had to be progressively refined for each angle of attack in order to properly resolve the boundary layer. The factor f that multiplies the maximum subsonic layer thickness was decreased from 1.8 (2.5 deg case) to 1.25 (10 deg case) to maintain reasonable marching stepsizes. In each case the grid lines were placed orthogonal to the body. The starting solution was marched up to an axial location of $x = 2.5$. Since there is a paucity of experimental data in such severe hypersonic regimes, the results of these calculations are simply compared against the results of the zero degree calculations.

The computed results for this test case are too numerous to show in their entirety. Instead, only a representative sampling of the results is presented. In order to provide greater details of the flow field, only 50 percent of the solution domain is shown in the figures that follow. The effect of angle of attack on the temperature is depicted in Figs. 13a-13d. The temperature profiles in the pitch plane of symmetry are shown in these figures. The following observations can be made from these figures: (i) the boundary layer thickens considerably on the leeside while thinning on the windside, (ii) the edge temperatures increase rapidly on the windside while decreasing gradually on the leeside, and (iii) the peak temperatures decrease on the leeside but stay very nearly the same on the windside. The shock on the leeside weakens and begins to smear. At the highest angle of the attack the shock cannot be discerned from the figure. This is due to a combination of central-differencing and coarseness of the grid.

In Figs. 14a-14d, the effect of angle of attack on the mass fraction atomic oxygen in the pitch plane is shown. The amount of atomic oxygen at the wall decreases with increasing angle of attack. However, due to diffusional effects atomic oxygen is present over a larger distance from the body. On the windside, the amount of atomic oxygen increases at the wall but is present over a smaller distance.

For different angles of attack, the axial variation of the surface pressure and Stanton number on the windward and leeward meridians is shown in Figs. 15a-15d and Figs. 16a-16d, respectively. The increase in surface pressure and heat transfer on the windside and the decrease on the leeside with increasing angle of attack is evident from these figures.

The computations were performed on either the CRAY-XMP/48 or the CRAY-2 (NAS) computers at NASA Ames Research Center. Each test case involved 10 x 10 block matrices and required 4.3 milliseconds per grid point per step on the CRAY-XMP computer. The first test case required 2000 steps and the second test case required 1800 steps for the lowest angle of attack calculation to 600 steps for the highest angle of attack calculation.

Concluding Remarks

A new PNS code was developed to compute hypersonic laminar flow of chemically reacting air consisting of six species and electrons. The species were treated as calorically imperfect but thermally perfect gases. A noniterative, implicit, approximately-factored, space-marching method was used to solve the coupled set of gas dynamic and species conservation equations. In order to validate the code, two test cases were computed. The first test case was that of hypersonic flow over a 10 deg. cone at 0 deg. angle of attack. The results of this calculation were compared against those of a reacting boundary-layer code. The agreement was found to be very good. These results were further shown to lie between two extremes (ideal gas and equilibrium air). The second test computed was that of hypersonic laminar flow of reacting air over a 10 deg. cone at several angles of attack. Due to the unavailability of experimental data for this case, the numerical results were simply compared against the results of the 0 deg. calculation. These calculations were performed not only to demonstrate the three-dimensional capabilities of the code but also to provide "benchmark" calculations for future code developers. Work is currently being done in the area of shock fitting. A simple turbulence model (Cebeci-Smith) has also been incorporated into the present code and this option remains to be validated. The present study indicates that there is a need for a comprehensive experimental database for validation of nonequilibrium codes.

Acknowledgements

This work was supported by NASA Ames Research Center under Grant NAG-2-245 and the Computational Fluid Dynamics Center, Iowa State University, Ames, Iowa.

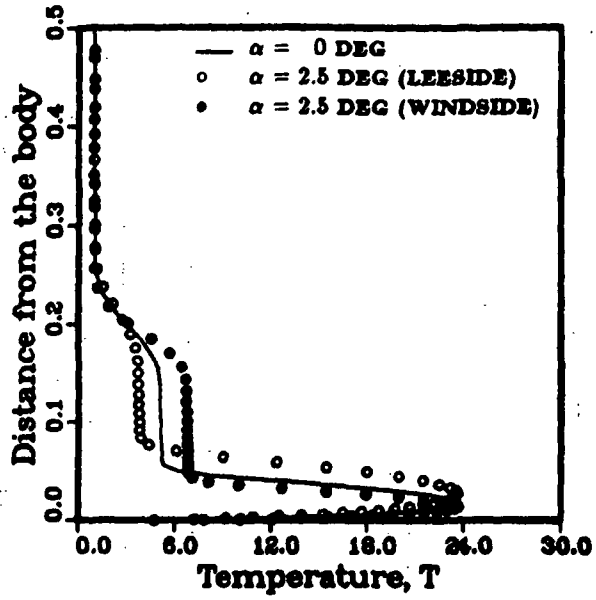

Fig. 13a

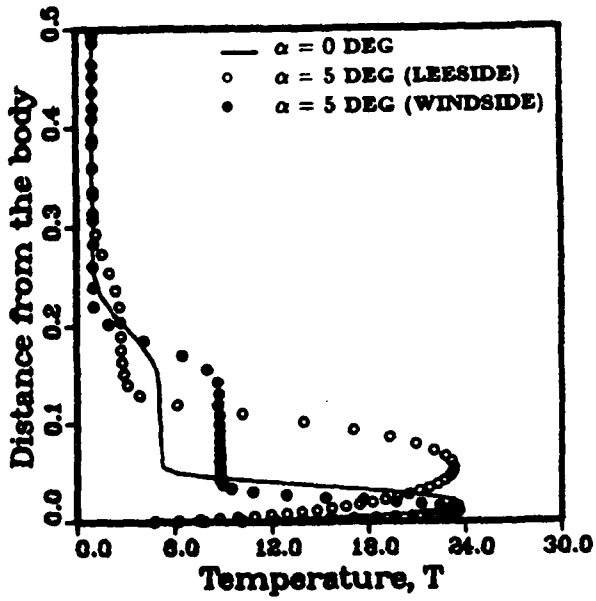

Fig. 13b

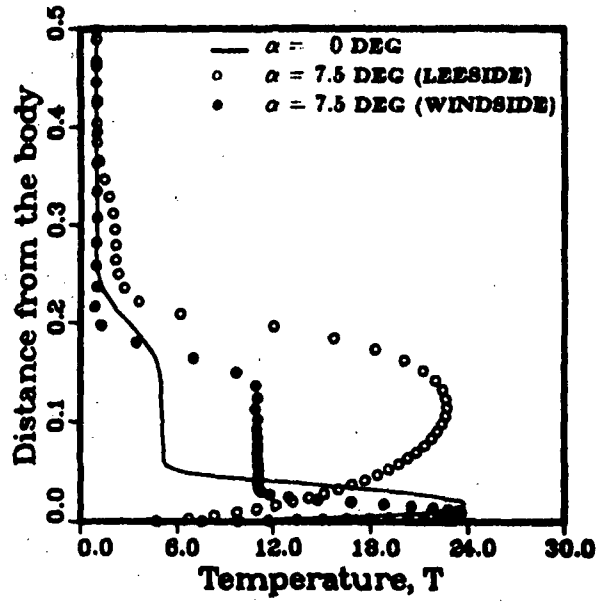

Fig. 13c

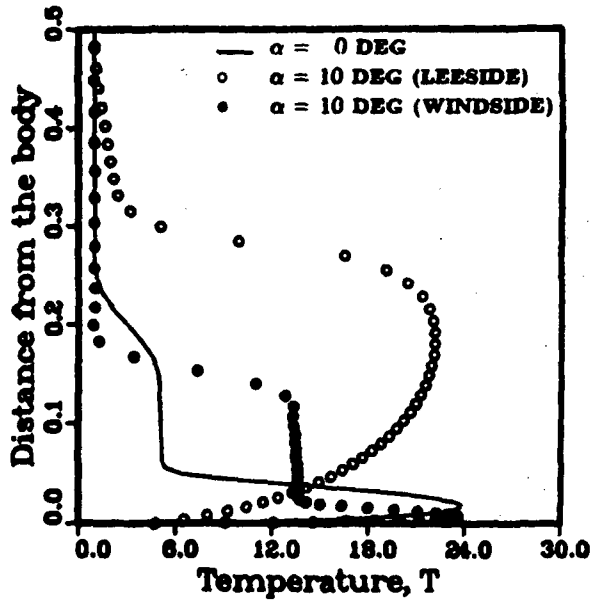

Fig. 13d

Fig. 13 Effect of angle of attack on temperature.
Pitch plane temperature profiles at $x = 3.5$.
(a) $\alpha = 2.5$ deg, (b) $\alpha = 5$ deg,
(c) $\alpha = 7.5$ deg, (d) $\alpha = 10$ deg.

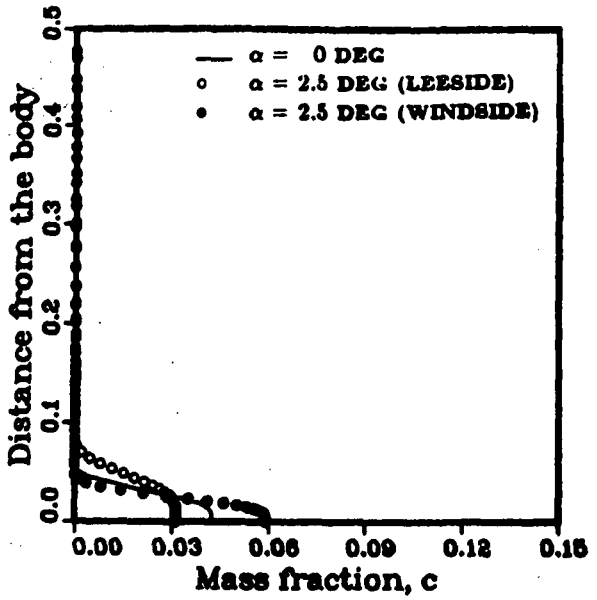

Fig. 14a

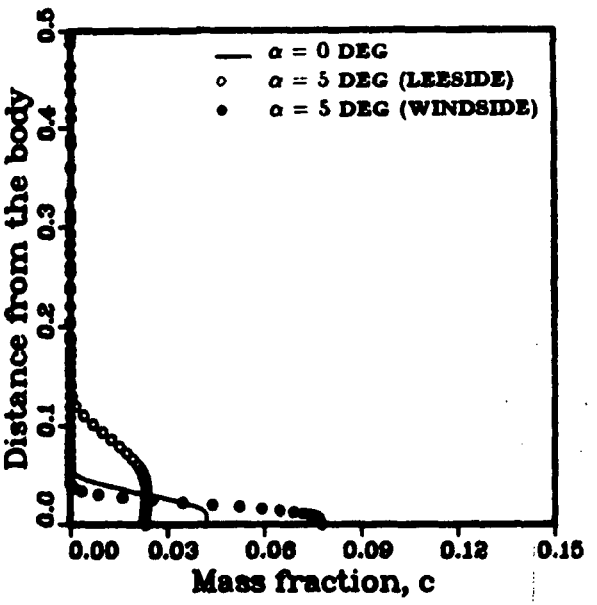

Fig. 14b

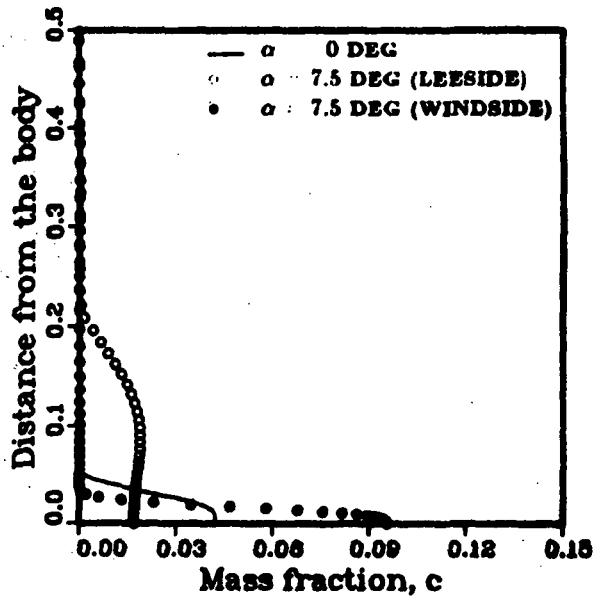

Fig. 14c

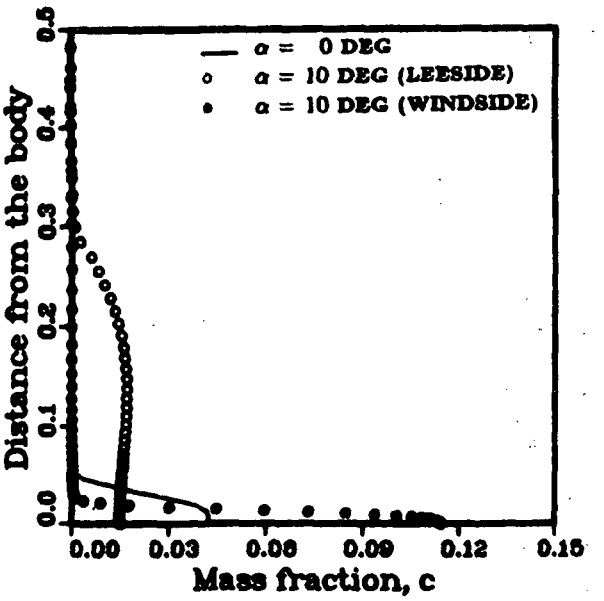

Fig. 14d

Fig. 14 Effect of angle of attack on chemistry.
Pitch plane O mass fraction profiles at $x = 3.5$.
(a) $\alpha = 2.5$ deg, (b) $\alpha = 5$ deg,
(c) $\alpha = 7.5$ deg, (d) $\alpha = 10$ deg.

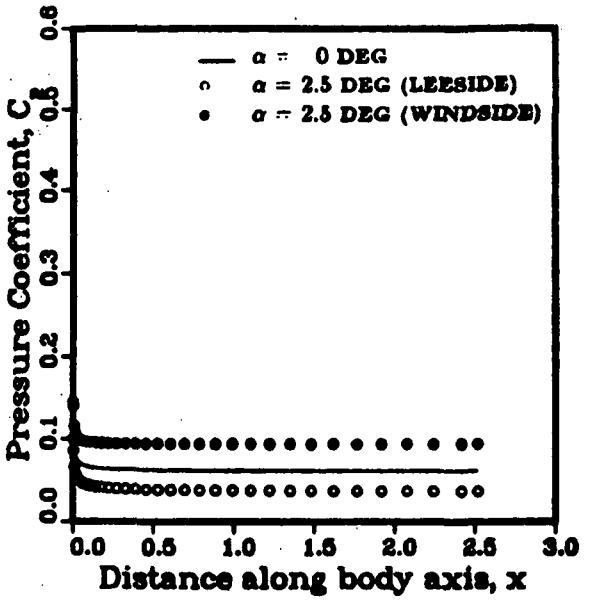

Fig. 15a

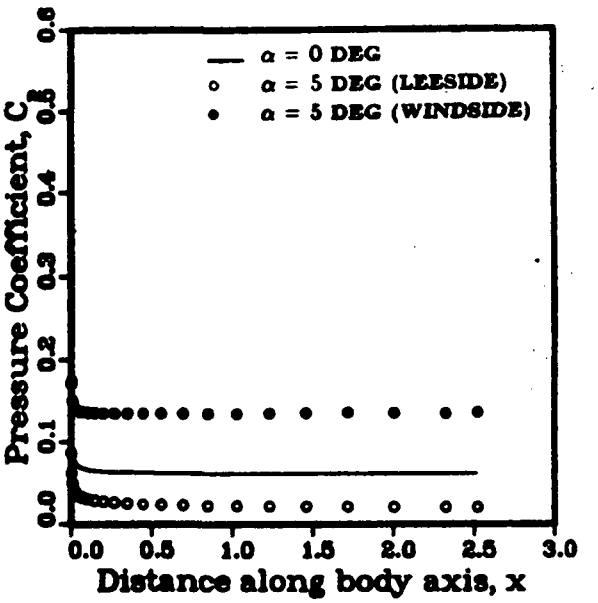

Fig. 15b

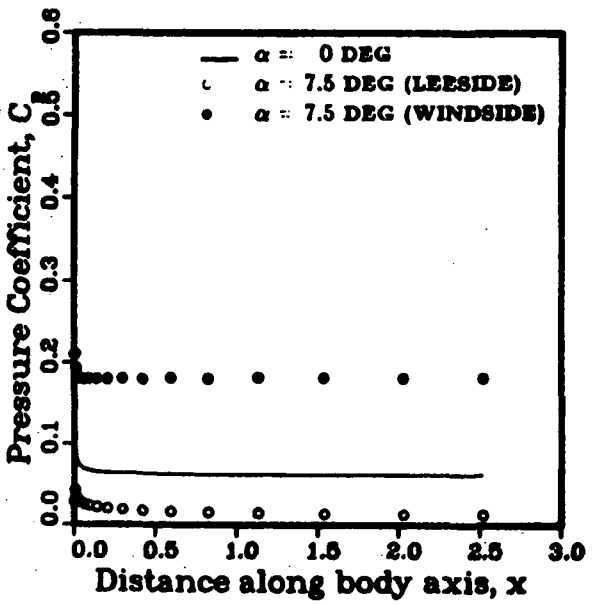

Fig. 15c

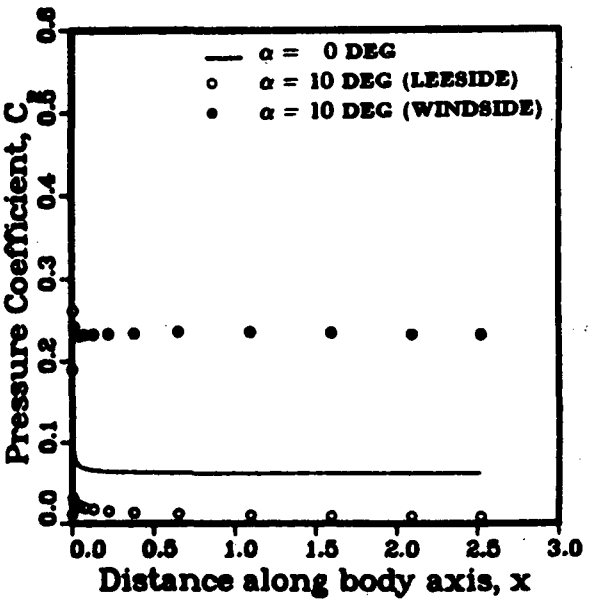

Fig. 15d

Fig. 15 Effect of angle of attack on surface pressure. Axial variation of surface pressure coefficient. (a) α = 2.5 deg, (b) α = 5 deg, (c) α = 7.5 deg, (d) α = 10 deg.

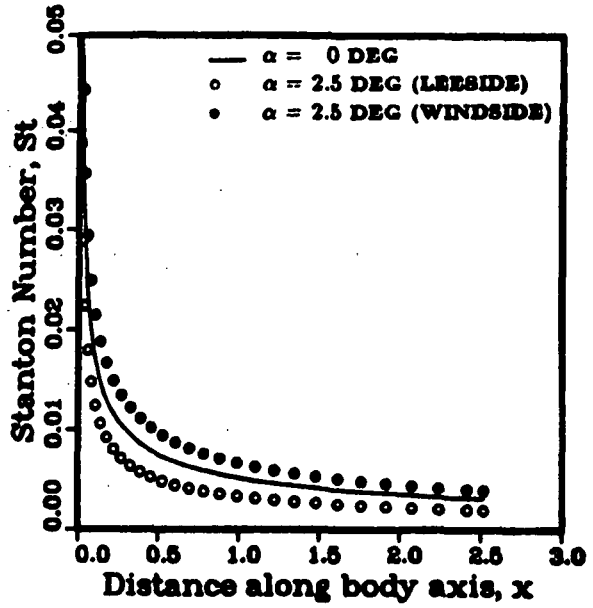

Fig. 16a

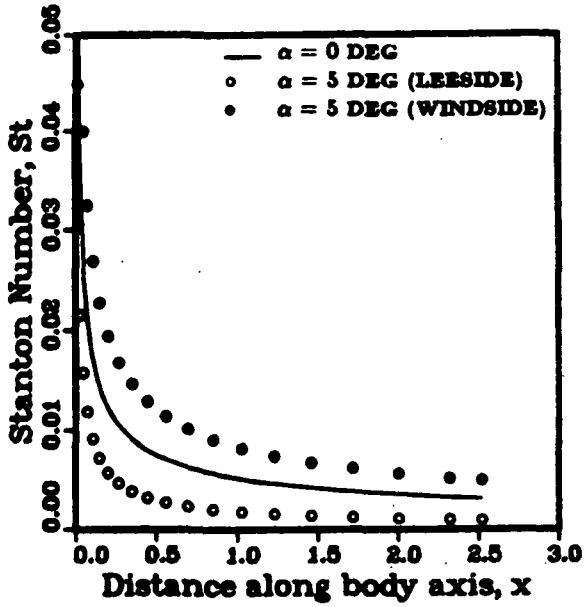

Fig. 16b

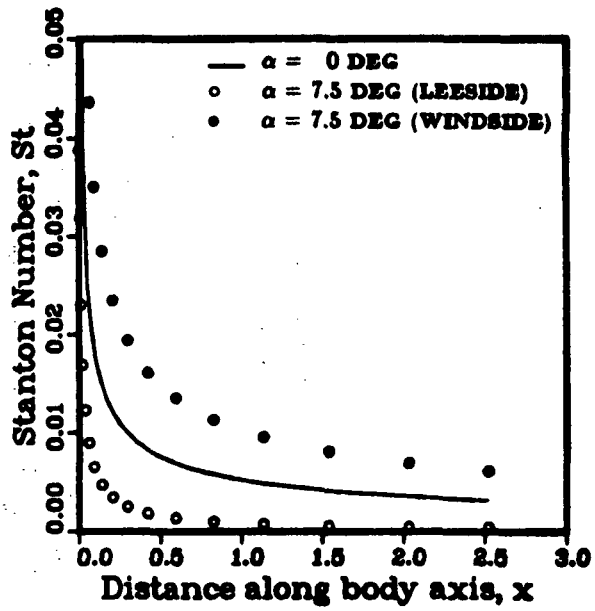

Fig. 16c

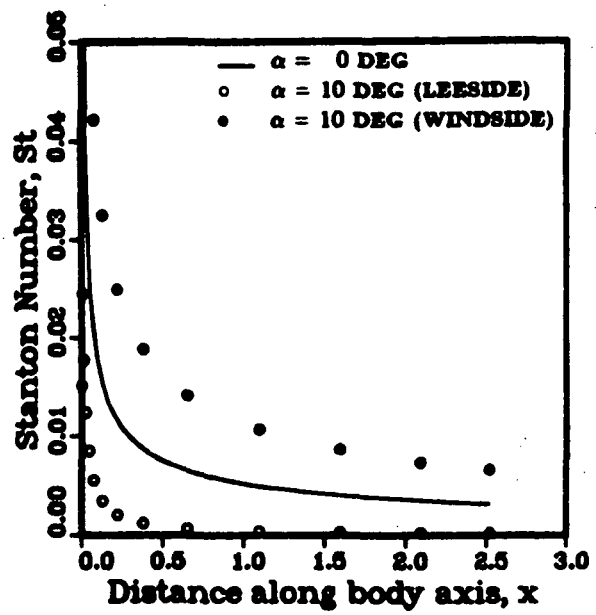

Fig. 16d

Fig. 16 Effect of angle of attack on heat transfer.
Axial variation of Stanton number.
(a) α = 2.5 deg, (b) α = 5 deg,
(c) α = 7.5 deg, (d) α = 10 deg.

References

1. Walberg, G. D., "A Survey of Aeroassisted Orbit Transfer," Journal of Spacecraft and Rockets, Vol. 22, No. 1., Jan.-Feb. 1985, pp. 3-18.
2. Howe, J. T., "Introductory Aerothermodynamics of Advanced Space Transportation Systems," Journal of Spacecraft and Rockets, Vol. 22, No. 1, Jan.-Feb. 1985, pp. 104-111.
3. Park, C., "Problems of Rate Chemistry in the Flight Regimes of Aeroassisted Orbital Transfer Vehicles," Thermal Design of Aeroassisted Orbit Transfer Vehicles, ed. H. F. Nelson, Progress in Aeronautics and Astronautics, Vol. 96, 1985, pp. 511-537.
4. Park, C., "On Convergence of Computation of Chemically Reacting Flows," AIAA Paper No. 85-0247, Jan. 1985.
5. Gnoffo, P. A. and McCandless, R. S., "Three-Dimensional AOTV Flowfields in Chemical Nonequilibrium," AIAA Paper No. 86-0230, Jan. 1986.
6. Gnoffo, P. A., McCandless, R. S., and Yee, H. C., "Enhancement to Program LAURA for Computation of Three-Dimensional Hypersonic Flow," AIAA Paper No. 87-0280, Jan. 1987.
7. Li, C. P., "Implicit Methods for Computing Chemically Reacting Flow," NASA TM-58274, Sept. 1986.
8. Li, C. P., "Chemistry Split Techniques for Viscous Reactive Blunt Body Flow Computations," AIAA Paper No. 87-0282, Jan. 1987.
9. Shinn, J. L., Moss, J. N., and Simmonds, A. L., "Viscous-Shock-Layer Heating Analysis for the Shuttle Windward Plane with Surface Finite Catalytic Recombination Rate," AIAA Paper No. 84-0842, June 1982.
10. Swaminathan, S., Kim, M. D., and Lewis, C. H., "Nonequilibrium Viscous Shock-Layer Flows over Blunt Sphere-Cones at Angles-of-Attack," AIAA Paper No. 82-0825,June 1982.
11. Bhutta, B. A., Lewis, C. H., and Kautz, F. A., II, "A Fast Fully-Iterative Parabolized Navier-Stokes Scheme for Chemically-Reacting Reentry Flows," AIAA Paper No. 85-0926, June 1985.
12. Prabhu, D. K., Tannehill, J. C., and Marvin, J. G., "A New PNS Code for Chemical Nonequilibrium Flows," AIAA Paper No. 87-0248, Jan. 1987.
13. Blottner, F. G., Johnson, M., and Ellis, M., "Chemically Reacting Viscous Flow Program for Multi-Component Gas Mixtures," Report No. SC-RR-70-754, Sandia Laboratories, Albuquerque, New Mexico, Dec. 1971.
14. Lee, J. H., "Basic Governing Equations for the Flight Regimes of Aeroassisted Orbital Transfer Vehicles," Thermal Design of Aeroassisted Orbital Transfer Vehicles, ed. H. F. Nelson, Progress in Aeronautics and Astronautics, Vol. 96, 1985, pp. 3-53.
15. Wilke, C. R., "A Viscosity Equation for Gas Mixtures," J. Chem. Phys., Vol. 18, No. 4, Apr. 1950, p. 517.
16. Vigneron. Y. C., Rakich, J. V., and Tannehill, J. C., "Calculation of Supersonic Flow over Delta Wings with Sharp Subsonic Leading Edges," AIAA Paper No. 78-1137, July 1978.
17. Tannehill, J. C., Venkatapathy, E., and Rakich, J. V., "Numerical Solution of Supersonic Viscous Flow over Blunt Delta Wings," AIAA J., Vol. 20, No. 2, Feb. 1982, pp. 203-210.
18. Steger, J. L., "Implicit Finite-Difference Simulation of Flow About Arbitrary Geometries with Applications to Airfoils," AIAA Paper No. 77-665, June 1977.
19. Schiff, L. B. and Steger, J. L., "Numerical Simulation of Steady Supersonic Viscous Flow," AIAA Paper No. 79-0130, January 1979.
20. Prabhu, D. K. and Tannehill, J. C., "Numerical Solution of Space Shuttle Orbiter Flowfield Including Real-Gas Effects," Journal of Spacecraft and Rockets, Vol. 23, No. 3, May-June 1986, pp. 264-272.
21. Srinivasan, S., Tannehill, J. C., and Weilmuenster, K. J., "Simplified Curve Fits for the Thermodynamic Properties of Equilibrium Air," ISU-ERI Report No. 86401, Iowa State University, Ames, Iowa, June 1986.

Appendix A: Fluxes and Source Terms

(a) Fluxes

The $(n+4)$-component inviscid flux vectors $\mathbf{E}^i$, $\mathbf{F}^i$, and $\mathbf{G}^i$ are

$$\begin{aligned}
\mathbf{E}^i &= \{\rho u, \rho u^2 + p, \rho uv, \rho uw, \rho uH, \rho uc_1, \rho uc_2, \ldots, \rho uc_{n-1}\}^T \\
\mathbf{F}^i &= \{\rho v, \rho uv, \rho v^2 + p, \rho vw, \rho vH, \rho vc_1, \rho vc_2, \ldots, \rho vc_{n-1}\}^T \\
\mathbf{G}^i &= \{\rho w, \rho uw, \rho vw, \rho w^2 + p, \rho wH, \rho wc_1, \rho wc_2, \ldots, \rho wc_{n-1}\}^T
\end{aligned} \tag{A1}$$

and the $(n+4)$-component viscous flux vectors $\mathbf{E}^v$, $\mathbf{F}^v$, and $\mathbf{G}^v$ are

$$\begin{aligned}
\mathbf{E}^v &= \{0, \tau^{xx}, \tau^{xy}, \tau^{xz}, u\tau^{xx} + v\tau^{xy} + w\tau^{xz} - q^x, m_1^x, m_2^x, \ldots, m_{n-1}^x\}^T \\
\mathbf{F}^v &= \{0, \tau^{yx}, \tau^{yy}, \tau^{yz}, u\tau^{yx} + v\tau^{yy} + w\tau^{yz} - q^y, m_1^y, m_2^y, \ldots, m_{n-1}^y\}^T \\
\mathbf{G}^v &= \{0, \tau^{zx}, \tau^{zy}, \tau^{zz}, u\tau^{zx} + v\tau^{zy} + w\tau^{zz} - q^z, m_1^z, m_2^z, \ldots, m_{n-1}^z\}^T
\end{aligned} \tag{A2}$$

The expressions for the components of the shear stress tensor, the heat flux vector and the diffusion mass flux vector are given below

$$\begin{aligned}
\tau^{xx} &= \frac{2}{3}\mu(2u_x - v_y - w_z) & q^x &= -\beta_2\kappa T_x - \sum_s [h_s - h_n] m_s^x \\
\tau^{yy} &= \frac{2}{3}\mu(-u_x + 2v_y - w_z) & q^y &= -\beta_2\kappa T_y - \sum_s [h_s - h_n] m_s^y \\
\tau^{zz} &= \frac{2}{3}\mu(-u_x - v_y + 2w_z) & q^z &= -\beta_2\kappa T_z - \sum_s [h_s - h_n] m_s^z \\
\tau^{xy} &= \mu(u_y + v_x) & m_s^x &= \beta_3\rho\mathcal{D}(c_s)_x \\
\tau^{xz} &= \mu(u_z + w_x) & m_s^y &= \beta_3\rho\mathcal{D}(c_s)_y \\
\tau^{yz} &= \mu(v_z + w_y) & m_s^z &= \beta_3\rho\mathcal{D}(c_s)_z
\end{aligned} \tag{A3}$$

The chemical source vector $\mathbf{W}^c$ is

$$\mathbf{W}^c = \{0, 0, 0, 0, 0, \dot{w}_1, \dot{w}_2, \ldots, \dot{w}_s, \ldots, \dot{w}_{n-1}\}^T \tag{A4}$$

where $\dot{w}_s$ is the mass production or depletion rate of species s.

(b) Chemical Source Terms

Consider a multicomponent system of n species undergoing m simultaneous elementary reactions. Let n_t be the total number of reactants. These reactions can be represented symbolically as

$$\sum_{l=1}^{n_t} \nu'_{k,l} A_l \rightleftharpoons \sum_{l=1}^{n_t} \nu''_{k,l} A_l \qquad k = 1, 2, \ldots, m$$

where $\nu'_{k,l}, \nu''_{k,l}$ are the stoichiometric coefficients and A_l is the chemical symbol of the lth species. Using the law of mass action, the nondimensional mass production rate of species s is

$$\dot{w}_s = M_s \sum_{k=1}^{m} (\nu''_{k,s} - \nu'_{k,s}) \left\{ K_{f,k}(T) \prod_{r=1}^{n_t} [\rho\gamma_r]^{\nu'_{k,r}} - K_{b,k}(T) \prod_{r=1}^{n_t} [\rho\gamma_r]^{\nu''_{k,r}} \right\} \tag{A5}$$

The nondimensional mole-mass ratios of the reactants are defined as

$$\gamma_r = \begin{cases} c_r / M_r & r = 1, 2, \ldots, n \\ \sum_{s=1}^{n} Z_{(r-n),s}\gamma_s & r = n+1, n+2, \ldots, n_t \end{cases} \tag{A6}$$

The reaction rates are functions of temperature and are expressed in the modified Arrhenius form, where the nondimensional forward and backward rates are written as

$$K_{f,k}(T) = \exp(\log_e C'_{1,k} + \frac{C'_{2,k}}{T} + C_{3,k}\log_e T) \tag{A7}$$

$$K_{b,k}(T) = \exp(\log_e D'_{1,k} + \frac{D'_{2,k}}{T} + D_{3,k}\log_e T) \tag{A8}$$

where

$$C'_{1,k} = \frac{L^*}{V^*_\infty} \left(\frac{\rho^*_\infty}{M^*_\infty} \right)^{\alpha_k - 1} 10^{3 - 3\alpha_k} T_\infty^{*C_{3,k}} C_{1,k}, \qquad C'_{2,k} = \frac{C_{2,k}}{T^*_\infty} \tag{A9}$$

$$D'_{1,k} = \frac{L^*}{V^*_\infty} \left(\frac{\rho^*_\infty}{M^*_\infty} \right)^{\beta_k - 1} 10^{3 - 3\beta_k} T_\infty^{*D_{3,k}} D_{1,k}, \qquad D'_{2,k} = \frac{D_{2,k}}{T^*_\infty} \tag{A10}$$

$$\alpha_k = \sum_{r=1}^{n_r} \nu'_{k,r}, \qquad \beta_k = \sum_{r=1}^{n_r} \nu''_{k,r} \tag{A11}$$

and $C_{1,k}$, $C_{2,k}$, $C_{3,k}$, $D_{1,k}$, $D_{2,k}$, and $D_{3,k}$ are constants for a particular reaction k.

(c) Transformed Fluxes

Under the coordinate transformation, Eq. 18, the transformed fluxes and source vectors are given by

$$\begin{aligned}
\hat{\mathbf{E}}^i &= (\tfrac{\xi_x}{J})\mathbf{E}^i + (\tfrac{\xi_y}{J})\mathbf{F}^i + (\tfrac{\xi_z}{J})\mathbf{G}^i & \hat{\mathbf{E}}^v &= (\tfrac{\xi_x}{J})\mathbf{E}^v + (\tfrac{\xi_y}{J})\mathbf{F}^v + (\tfrac{\xi_z}{J})\mathbf{G}^v \\
\hat{\mathbf{F}}^i &= (\tfrac{\eta_x}{J})\mathbf{E}^i + (\tfrac{\eta_y}{J})\mathbf{F}^i + (\tfrac{\eta_z}{J})\mathbf{G}^i & \hat{\mathbf{F}}^v &= (\tfrac{\eta_x}{J})\mathbf{E}^v + (\tfrac{\eta_y}{J})\mathbf{F}^v + (\tfrac{\eta_z}{J})\mathbf{G}^v \\
\hat{\mathbf{G}}^i &= (\tfrac{\zeta_x}{J})\mathbf{E}^i + (\tfrac{\zeta_y}{J})\mathbf{F}^i + (\tfrac{\zeta_z}{J})\mathbf{G}^i & \hat{\mathbf{G}}^v &= (\tfrac{\zeta_x}{J})\mathbf{E}^v + (\tfrac{\zeta_y}{J})\mathbf{F}^v + (\tfrac{\zeta_z}{J})\mathbf{G}^v \\
\hat{\mathbf{W}}^c &= (\tfrac{1}{J})\mathbf{W}^c & J &= \frac{\partial(\xi,\eta,\zeta)}{\partial(x,y,z)}
\end{aligned} \tag{A12}$$

where J is the Jacobian of the coordinate transformation.

The $(n+4)$-component transformed viscous flux vector, $\hat{\mathbf{F}}^v$, for the thin-layer approximation is

$$\hat{\mathbf{F}}^v = J \begin{pmatrix} 0 \\ \ell_1 u_\eta + \ell_4 v_\eta + \ell_5 w_\eta \\ \ell_4 u_\eta + \ell_2 v_\eta + \ell_6 w_\eta \\ \ell_5 u_\eta + \ell_6 v_\eta + \ell_3 w_\eta \\ \frac{1}{2}(\ell_1 - \ell_7)(u^2)_\eta + \frac{1}{2}(\ell_2 - \ell_7)(v^2)_\eta + \frac{1}{2}(\ell_3 - \ell_7)(w^2)_\eta + \\ \ell_4(uv)_\eta + \ell_5(uw)_\eta + \ell_6(vw)_\eta + \ell_7 H_\eta + (\ell_8 - \ell_7)\sum_s |h_s - h_n|(c_s)_\eta \\ \ell_8(c_1)_\eta \\ \ell_8(c_2)_\eta \\ \vdots \\ \ell_8(c_{n-1})_\eta \end{pmatrix} \tag{A13}$$

where the coefficients $\ell_1, \ell_2, \ldots, \ell_8$ are

$$\begin{aligned}
\ell_1 &= \mu\left[\frac{4}{3}(\tfrac{\eta_x}{J})^2 + (\tfrac{\eta_y}{J})^2 + (\tfrac{\eta_z}{J})^2\right] & \ell_5 &= \frac{\mu}{3}\left[(\tfrac{\eta_x}{J})(\tfrac{\eta_z}{J})\right] \\
\ell_2 &= \mu\left[(\tfrac{\eta_x}{J})^2 + \frac{4}{3}(\tfrac{\eta_y}{J})^2 + (\tfrac{\eta_z}{J})^2\right] & \ell_6 &= \frac{\mu}{3}\left[(\tfrac{\eta_y}{J})(\tfrac{\eta_z}{J})\right] \\
\ell_3 &= \mu\left[(\tfrac{\eta_x}{J})^2 + (\tfrac{\eta_y}{J})^2 + \frac{4}{3}(\tfrac{\eta_z}{J})^2\right] & \ell_7 &= \frac{\beta_2 \kappa}{C_{p_f}}\left[(\tfrac{\eta_x}{J})^2 + (\tfrac{\eta_y}{J})^2 + (\tfrac{\eta_z}{J})^2\right] \\
\ell_4 &= \frac{\mu}{3}\left[(\tfrac{\eta_x}{J})(\tfrac{\eta_y}{J})\right] & \ell_8 &= \beta_3 \rho D\left[(\tfrac{\eta_x}{J})^2 + (\tfrac{\eta_y}{J})^2 + (\tfrac{\eta_z}{J})^2\right]
\end{aligned} \tag{A14}$$

(d) Geometrical Parameters

The Jacobian and the metrics of the coordinate transformation are

$$J = \left[x_\xi(y_\eta z_\zeta - y_\zeta z_\eta) + x_\eta(y_\zeta z_\xi - y_\xi z_\zeta) + x_\zeta(y_\xi z_\eta - y_\eta z_\xi)\right]^{-1} \tag{A15}$$

$$\begin{aligned}
\frac{\xi_x}{J} &= (y_\eta z_\zeta - y_\zeta z_\eta) & \frac{\xi_y}{J} &= (x_\zeta z_\eta - x_\eta z_\zeta) & \frac{\xi_z}{J} &= (x_\eta y_\zeta - x_\zeta y_\eta) \\
\frac{\eta_x}{J} &= (y_\zeta z_\xi - y_\xi z_\zeta) & \frac{\eta_y}{J} &= (x_\xi z_\zeta - x_\zeta z_\xi) & \frac{\eta_z}{J} &= (x_\zeta y_\xi - x_\xi y_\zeta) \\
\frac{\zeta_x}{J} &= (y_\xi z_\eta - y_\eta z_\xi) & \frac{\zeta_y}{J} &= (x_\eta z_\xi - x_\xi z_\eta) & \frac{\zeta_z}{J} &= (x_\xi y_\eta - x_\eta y_\xi)
\end{aligned} \tag{A16}$$

Appendix B: Inviscid Jacobians

The inviscid Jacobian is an $(n+4)$ x $(n+4)$ matrix. The expressions for the elements of this matrix are given below.

Define the following quantities

$$\phi_s = \begin{cases} MC_{p_f}T(1/M_s - 1/M_n) - (h_s - h_n) & \text{if } s < n; \\ MC_{p_f}T(1/M_n) - h_n & \text{if } s = n. \end{cases} \tag{B1}$$

$$\hat{S}_x = \frac{S_x}{j}, \qquad \hat{S}_y = \frac{S_y}{j}, \qquad \hat{S}_z = \frac{S_z}{j} \tag{B2}$$

$$\hat{U} = \hat{S}_x u + \hat{S}_y v + \hat{S}_z w \tag{B3}$$

(a) Global Continuity

$$\begin{aligned} \hat{\mathbf{A}}_{1,2} &= \hat{S}_x \\ \hat{\mathbf{A}}_{1,3} &= \hat{S}_y \\ \hat{\mathbf{A}}_{1,4} &= \hat{S}_z \end{aligned} \tag{B4}$$

(b) ξ-Momentum

$$\begin{aligned} \hat{\mathbf{A}}_{2,1} &= -u\hat{U} + \omega\chi\hat{S}_x\left(\frac{V^2}{2} + \phi_n\right) \\ \hat{\mathbf{A}}_{2,2} &= (1-\omega\chi)\hat{S}_x u + \hat{U} \\ \hat{\mathbf{A}}_{2,3} &= \hat{S}_y u - \omega\chi\hat{S}_x v \\ \hat{\mathbf{A}}_{2,4} &= \hat{S}_z u - \omega\chi\hat{S}_x w \\ \hat{\mathbf{A}}_{2,5} &= \omega\chi\hat{S}_x \end{aligned} \qquad \begin{aligned} \hat{\mathbf{A}}_{2,6} &= \omega\chi\hat{S}_x\phi_1 \\ \hat{\mathbf{A}}_{2,7} &= \omega\chi\hat{S}_x\phi_2 \\ &\vdots \\ \hat{\mathbf{A}}_{2,n+4} &= \omega\chi\hat{S}_x\phi_{n-1} \end{aligned} \tag{B5}$$

(c) η-Momentum

$$\begin{aligned} \hat{\mathbf{A}}_{3,1} &= -v\hat{U} + \omega\chi\hat{S}_y\left(\frac{V^2}{2} + \phi_n\right) \\ \hat{\mathbf{A}}_{3,2} &= \hat{S}_x v - \omega\chi\hat{S}_y u \\ \hat{\mathbf{A}}_{3,3} &= (1-\omega\chi)\hat{S}_y v + \hat{U} \\ \hat{\mathbf{A}}_{3,4} &= \hat{S}_z v - \omega\chi\hat{S}_y w \\ \hat{\mathbf{A}}_{3,5} &= \omega\chi\hat{S}_y \end{aligned} \qquad \begin{aligned} \hat{\mathbf{A}}_{3,6} &= \omega\chi\hat{S}_y\phi_1 \\ \hat{\mathbf{A}}_{3,7} &= \omega\chi\hat{S}_y\phi_2 \\ &\vdots \\ \hat{\mathbf{A}}_{3,n+4} &= \omega\chi\hat{S}_y\phi_{n-1} \end{aligned} \tag{B6}$$

(d) ζ-Momentum

$$\begin{aligned} \hat{\mathbf{A}}_{4,1} &= -w\hat{U} + \omega\chi\hat{S}_z\left(\frac{V^2}{2} + \phi_n\right) \\ \hat{\mathbf{A}}_{4,2} &= \hat{S}_x w - \omega\chi\hat{S}_z u \\ \hat{\mathbf{A}}_{4,3} &= \hat{S}_y w - \omega\chi\hat{S}_z v \\ \hat{\mathbf{A}}_{4,4} &= (1-\omega\chi)\hat{S}_z w + \hat{U} \\ \hat{\mathbf{A}}_{4,5} &= \omega\chi\hat{S}_z \end{aligned} \qquad \begin{aligned} \hat{\mathbf{A}}_{4,6} &= \omega\chi\hat{S}_z\phi_1 \\ \hat{\mathbf{A}}_{4,7} &= \omega\chi\hat{S}_z\phi_2 \\ &\vdots \\ \hat{\mathbf{A}}_{4,n+4} &= \omega\chi\hat{S}_z\phi_{n-1} \end{aligned} \tag{B7}$$

(e) Energy

$$\begin{aligned} \hat{\mathbf{A}}_{5,1} &= -\hat{U}H \\ \hat{\mathbf{A}}_{5,2} &= \hat{S}_x H \\ \hat{\mathbf{A}}_{5,3} &= \hat{S}_y H \\ \hat{\mathbf{A}}_{5,4} &= \hat{S}_z H \\ \hat{\mathbf{A}}_{5,5} &= \hat{U} \end{aligned} \tag{B8}$$

(f) Species Continuity ($s = 1, 2, \ldots, n-1$)

$$\begin{aligned} \hat{\mathbf{A}}_{5+s,1} &= -\hat{U}c_s \\ \hat{\mathbf{A}}_{5+s,2} &= \hat{S}_x c_s \\ \hat{\mathbf{A}}_{5+s,3} &= \hat{S}_y c_s \\ \hat{\mathbf{A}}_{5+s,4} &= \hat{S}_z c_s \\ \hat{\mathbf{A}}_{5+s,5+s} &= \hat{U} \end{aligned} \tag{B9}$$

Notes

(1) The elements not listed above are identically zero.

(2) The elements of the inviscid Jacobian $\partial\hat{\mathbf{E}}'/\partial\mathbf{Q}$ are obtained by setting $S_x = \xi_x$, $S_y = \xi_y$ and $S_z = \xi_z$.

(3) The elements of the inviscid Jacobian $\partial\hat{\mathbf{F}}'/\partial\mathbf{Q}$ are obtained by setting $S_x = \eta_x$, $S_y = \eta_y$, $S_z = \eta_z$, and $\omega = 1$.

(4) The elements of the inviscid Jacobian $\partial\hat{\mathbf{G}}'/\partial\mathbf{Q}$ are obtained by setting $S_x = \zeta_x$, $S_y = \zeta_y$, $S_z = \zeta_z$, and $\omega = 1$.

Appendix C: Viscous Jacobian

The viscous Jacobian is also an $(n + 4) \times (n + 4)$ matrix. The expressions for the elements of this matrix are given below. The following notation is used

$$\psi_s = J\ell_s \qquad s = 1, 2, \ldots, 8 \tag{C1}$$

where $\ell_1, \ell_2, \ldots, \ell_8$ are defined in Eq. A14.

(a) ξ-Momentum

$$\begin{aligned}
\hat{\mathbf{M}}_{2,1} &= -\left[\psi_1\left(\frac{u}{\rho}\right)_\eta + \psi_4\left(\frac{v}{\rho}\right)_\eta + \psi_5\left(\frac{w}{\rho}\right)_\eta\right] \\
\hat{\mathbf{M}}_{2,2} &= \psi_1\left(\frac{1}{\rho}\right)_\eta \\
\hat{\mathbf{M}}_{2,3} &= \psi_4\left(\frac{1}{\rho}\right)_\eta \\
\hat{\mathbf{M}}_{2,4} &= \psi_5\left(\frac{1}{\rho}\right)_\eta
\end{aligned} \tag{C2}$$

(b) η-Momentum

$$\begin{aligned}
\hat{\mathbf{M}}_{3,1} &= -\left[\psi_4\left(\frac{u}{\rho}\right)_\eta + \psi_2\left(\frac{v}{\rho}\right)_\eta + \psi_6\left(\frac{w}{\rho}\right)_\eta\right] \\
\hat{\mathbf{M}}_{3,2} &= \psi_4\left(\frac{1}{\rho}\right)_\eta \\
\hat{\mathbf{M}}_{3,3} &= \psi_2\left(\frac{1}{\rho}\right)_\eta \\
\hat{\mathbf{M}}_{3,4} &= \psi_6\left(\frac{1}{\rho}\right)_\eta
\end{aligned} \tag{C3}$$

(c) ζ-Momentum

$$\begin{aligned}
\hat{\mathbf{M}}_{4,1} &= -\left[\psi_5\left(\frac{u}{\rho}\right)_\eta + \psi_6\left(\frac{v}{\rho}\right)_\eta + \psi_3\left(\frac{w}{\rho}\right)_\eta\right] \\
\hat{\mathbf{M}}_{4,2} &= \psi_5\left(\frac{1}{\rho}\right)_\eta \\
\hat{\mathbf{M}}_{4,3} &= \psi_6\left(\frac{1}{\rho}\right)_\eta \\
\hat{\mathbf{M}}_{4,4} &= \psi_3\left(\frac{1}{\rho}\right)_\eta
\end{aligned} \tag{C4}$$

(d) Energy

$$\begin{aligned}
\hat{\mathbf{M}}_{5,1} = -\Big[&(\psi_1 - \psi_7)\left(\frac{u^2}{\rho}\right)_\eta + (\psi_2 - \psi_7)\left(\frac{v^2}{\rho}\right)_\eta + (\psi_3 - \psi_7)\left(\frac{w^2}{\rho}\right)_\eta + 2\psi_4\left(\frac{uv}{\rho}\right)_\eta + \\
&2\psi_5\left(\frac{uw}{\rho}\right)_\eta + 2\psi_6\left(\frac{vw}{\rho}\right)_\eta + \psi_7\left(\frac{H}{\rho}\right)_\eta + (\psi_8 - \psi_7)(h_1 - h_n)\left(\frac{c_1}{\rho}\right)_\eta + \\
&(\psi_8 - \psi_7)(h_2 - h_n)\left(\frac{c_2}{\rho}\right)_\eta + \ldots + (\psi_8 - \psi_7)(h_{n-1} - h_n)\left(\frac{c_{n-1}}{\rho}\right)_\eta\Big] \\
\hat{\mathbf{M}}_{5,2} &= (\psi_1 - \psi_7)\left(\frac{u}{\rho}\right)_\eta + \psi_4\left(\frac{v}{\rho}\right)_\eta + \psi_5\left(\frac{w}{\rho}\right)_\eta \\
\hat{\mathbf{M}}_{5,3} &= \psi_4\left(\frac{u}{\rho}\right)_\eta + (\psi_2 - \psi_7)\left(\frac{v}{\rho}\right)_\eta + \psi_6\left(\frac{w}{\rho}\right)_\eta \\
\hat{\mathbf{M}}_{5,4} &= \psi_5\left(\frac{u}{\rho}\right)_\eta + \psi_6\left(\frac{v}{\rho}\right)_\eta + (\psi_3 - \psi_7)\left(\frac{w}{\rho}\right)_\eta
\end{aligned} \tag{C5}$$

$$\hat{M}_{5,5} = \psi_7(\frac{1}{\rho})_\eta$$

$$\hat{M}_{5,6} = (\psi_8 - \psi_7)(h_1 - h_n)(\frac{1}{\rho})_\eta$$

$$\vdots$$

$$\hat{M}_{5,n+4} = (\psi_8 - \psi_7)(h_{n-1} - h_n)(\frac{1}{\rho})_\eta$$

(e) Species Continuity ($s = 1, 2, \ldots, n-1$)

$$\begin{aligned} \hat{M}_{5+s,1} &= -\psi_8(\frac{c_s}{\rho})_\eta \qquad s = 1, 2, \ldots, n-1 \\ \hat{M}_{5+s,5+s} &= \psi_8(\frac{1}{\rho})_\eta \qquad s = 1, 2, \ldots, n-1 \end{aligned} \tag{C6}$$

Notes

(1) The elements not listed above are identically zero.
(2) $(\,)_\eta = \frac{\partial}{\partial \eta}(\,)$.

Appendix D: Source Term Jacobian

The chemical source vector, $\hat{\mathbf{W}}^c$, is a function of the mixture temperature, density, and mass concentrations. This is mathematically expressed as

$$\hat{\mathbf{W}}^c = \frac{1}{J}\mathbf{W}^c(T, \rho\gamma_1, \rho\gamma_2, \ldots, \rho\gamma_{n_r}) \tag{D1}$$

The Jacobian of the source term is

$$\hat{\mathbf{A}}^c = \frac{\partial \hat{\mathbf{W}}^c}{\partial \mathbf{Q}} = \frac{1}{J}\frac{\partial \mathbf{W}^c}{\partial \mathbf{Q}} \tag{D2}$$

Using Eq. *D*1 and the chain rule, the partial derivative in Eq. *D*2 can be written as

$$\frac{\partial \mathbf{W}^c}{\partial \mathbf{Q}} = \frac{\partial \mathbf{W}^c}{\partial T}\frac{\partial T}{\partial \mathbf{Q}} + \frac{\partial \mathbf{W}^c}{\partial \Gamma}\frac{\partial \Gamma}{\partial \mathbf{Q}} \tag{D3}$$

where Γ is the vector containing the mass concentrations of the reactants. The derivative $\partial \mathbf{W}^c/\partial T$ is easily evaluated since the reaction rate constants are the only quantities that depend explicitly on the temperature. The derivative $\partial T/\partial \mathbf{Q}$ is a $1 \times (n+4)$ row vector whose elements are

$$\frac{\partial T}{\partial \mathbf{Q}} = \frac{1}{\rho C_{p_f}}\left\{\frac{V^2}{2} - h_n, -u, -v, -w, 1, -(h_1 - h_n), -(h_2 - h_n), \ldots, -(h_{n-1} - h_n)\right\} \tag{D4}$$

Evaluation of the second term of Eq. *D*3 is little more involved. The derivative $\partial \mathbf{W}^c/\partial \Gamma$ is obtained by differentiating Eq. *A*5 with respect to the elements of Γ and the derivative $\partial \Gamma/\partial \mathbf{Q}$ is easily evaluated using Eq. *A*6.

The research performed during NASA Grant NAG 2-245 is described by the 7 documents listed below:

1. Prabhu, D.K. and Tannehill, J.C., "Numerical Solution of Space Shuttle Orbiter Flow Field Including Real Gas Effects," AIAA Paper 84-1747, June 1984.

2. Prabhu, D.K., "Numerical Solution of the Real Gas Flow Field Around the Space Shuttle Orbiter," M.S. Thesis, Iowa State University, Ames, Iowa, 1985.

3. Prabhu, D.K. and Tannehill, J.C., "Numerical Solution of Space Shuttle Orbiter Flowfield Including Real-Gas Effects," Journal of Spacecraft and Rockets, Vol. 23, No. 3, May-June 1986, pp. 264-272.

4. Prabhu, D.K., Tannehill, J.C., and Marvin, J.G., "A New PNS Code for Chemical Nonequilibrium Flows," AIAA Paper No. 87-0248, Jan. 1987.

5. Prabhu, D.K., Tannehill, J.C., and Marvin, J.G., "A New PNS Code for Three-Dimensional Chemically Reacting Flows," AIAA Paper 87-1472, Accepted for publication in Journal of Thermophysics and Heat Transfer.

6. Prabhu, D.K., "A New Parabolized Navier-Stokes Code for Chemically Reacting Flow Fields," Ph.D. Dissertation, Iowa State University, Ames, Iowa, 1987.

7. Prabhu, D.K., Tannehill, J.C., and Marvin, J.G., "A New PNS Code for Chemical Nonequilibrium Flows," AIAA Journal, To appear July or August 1988.